GEOPHYSICS, VOL. 69, NO. 4 (JULY-AUGUST 2004); P. 925–937, 14 FIGS.
10.1190/1.1778236

Three-dimensional regularized focusing inversion of gravity gradient tensor component data

Michael S. Zhdanov*, Robert Ellis‡, and Souvik Mukherjee*

ABSTRACT

We develop a new method for interpretation of tensor gravity field component data, based on regularized focusing inversion. The focusing inversion makes its possible to reconstruct a sharper image of the geological target than conventional maximum smoothness inversion. This new technique can be efficiently applied for the interpretation of gravity gradiometer data, which are sensitive to local density anomalies. The numerical modeling and inversion results show that the resolution of the gravity method can be improved significantly if we use tensor gravity data for interpretation. We also apply our method for inversion of the gradient gravity data collected by BHP Billiton over the Cannington Ag-Pb-Zn orebody in Queensland, Australia. The comparison with the drilling results demonstrates a remarkable correlation between the density anomaly reconstructed by the gravity gradient data and the true structure of the orebody. This result indicates that the emerging new geophysical technology of the airborne gravity gradient observations can improve significantly the practical effectiveness of the gravity method in mineral exploration.

INTRODUCTION

Gravity gradiometry involves measuring the gradient of a gravity field in different directions. We can consider three different components of a gravity field in some Cartesian coordinate system g_x, g_y, and g_z. The set of the x-, y-, and z-derivatives of each of these components forms the gravity gradient tensor.

The first practical instrument for measuring the horizontal derivative of the horizontal component of the gravity field and the derivative of the vertical component was designed in 1886 by the Hungarian physicist Baron von Eötvös. This instrument is known as the torsion balance gradiometer (Shaw and Lancaster-Jones, 1923, 1927). The Eötvös balance instrument signaled the advent of gravity gradiometry as an early geophysical method used successfully in resource exploration (Bell and Hansen, 1998; Pawlowski, 1998). During World War I, this instrument mapped salt domes associated with oil deposits in Germany, Hungary, and Czechoslavakia. Following World War I, word of Eötvös success rapidly reached the United States, and by 1922 Eötvös balances were imported by Shell and Amerada. The first discovery made by the torsion balance was the Nash Dome deposit in 1924. During the next 10 years or so, the discovery of more than 1 billion bbl oil and at least 79 producing structures was attributed to the application of this instrument (Bell and Hansen, 1998).

However, use of this instrument was both laborious and time consuming, involving leveling terrain in eight directions, often out to 100 m, and requiring a large tent in which the instrument was kept. Moreover, while early identification of salt domes and cap rocks was strikingly simple, with arrows resulting from the data pointing toward the salt dome, the arrow became more difficult to interpret over more complex structures. This, coupled with the absence of efficient interpretation tools involving modern-day modeling and inversion techniques, led to the demise of the static gradiometer as an investigative tool by the 1930s. Growing importance was attached to the simple pendulum gravitmeter, which, though significantly less accurate, was much faster and yielded data that most geologists found easier to interpret.

The modern era of gradiometry was born in the 1970s when Bell Aerospace (now Lockheed Martin) explored the feasibility of developing a moving base gravity gradiometer instrument (GGI). This work was originally stimulated by the personnel from Navoceano, who were using the Bell gradiometer to form the gravity field database for correction of ballistic missile submarine navigation systems (Metzger, 1977, 1982). The GGI design was based on four pendulous force rebalance accelerometers mounted on a slowly rotated fixture (Figure 1). These accelerometers measure the horizontal derivatives of the horizontal gravity field components.

Manuscript received by the Editor April 8, 2003; revised manuscript received January 21, 2004.
*University of Utah, Department of Geology and Geophysics, 135 South 1460 East, Room 719, Salt Lake City, Utah 84112. E-mail: mzhdanov@mines.utah.edu; smukherjee@mines.utah.edu.
‡BHP Billiton, Minerals Exploration, 1111 West Georgia Street, Suite 1400, Vancouver, British Columbia V6E 4M3, Canada. E-mail: robert.g.ellis@bhpbilliton.com.

With the introduction of the moving base gravity gradiometer, the great potential of the old technology for the mining and petroleum industry has come to realization again. In the 1990s BHP Billiton built the Falcon™ airborne gravity gradiometer (AGG), a derivative of the Bell GGI system. Routine airborne survey operations with the Falcon™ AGG system began in 1999 and 2000 (van Leeuwen, 2000; Lee, 2001). BHP Billiton reports that this instrument provides sufficient resolution and sensitivity for detecting the local gravity anomalies associated with mineral deposits (Christensen et al., 2001).

The development of the interpretive tools for gradiometer data still remains a challenge of the modern-day gradiometry. Some new techniques for gravity gradiometer data processing and interpretation have been reported, such as Condi and Talwani (1999), Jorgensen and Kisabeth (2000), Li (2001a,b), and Routh et al. (2001). However, most of the published methods are based on the traditional maximum smoothness inversion algorithms. Portniaguine and Zhdanov (1999, 2002) and Zhdanov (2002) have developed a focusing method for 3D gravity and magnetic data inversion based on the implementation of a new focusing stabilizer for regularized inversion of potential field data. Focusing inversion makes it possible to reconstruct a sharper image of the geological target than conventional maximum smoothness inversion. This new technique seems to be well suited for the interpretation of gravity gradiometer data, which are sensitive to local density anomalies (Zhdanov et al., 2002).

In the present paper, we extend this method for gravity gradiometer data inversion and for joint inversions of gravity and tensor gravity data. We also apply our new method for inversion of the gradient gravity data collected by BHP Billiton in the area of the Cannington Ag-Pb-Zn orebody in Queensland, Australia. The comparison of the inversion result with the drilling data shows remarkable resolving power of the new airborne technology in detecting the small, localized density anomaly and reconstructing the deep structure of the mineral deposit.

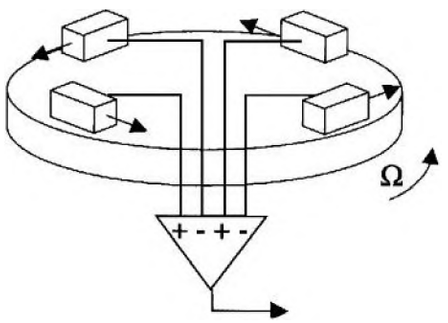

Figure 1. A moving base GGI is based on four pendulous force rebalance accelerometers mounted on a slowly rotated fixture so they are equispaced on a circle, with their sensitive axes tangential to the circle with the same sense. The fixture rotates at a constant speed, typically $\Omega = 0.25$ rad/s, providing a further ability for common mode rejection. The four accelerometers form a complement, and their outputs are combined (summed) so that orthogonal accelerometers have opposite sense and opposed accelerometers have the same sense (after Lee, 2001).

SECOND DERIVATIVES OF THE GRAVITY POTENTIAL

Gravity gradient tensor

For completeness, we begin with a brief description of the gravity gradient tensor. The gravity field $\mathbf{g}$, satisfies the equations (Zhdanov, 1988)

$$\nabla \cdot \mathbf{g} = -4\pi\gamma\rho, \quad \nabla \times \mathbf{g} = 0, \tag{1}$$

where γ is the universal gravitational constant and ρ is the anomalous density distribution within a domain D.

The solution of these equations is given by

$$\mathbf{g}(\mathbf{r}) = \gamma \iiint_D \rho(\mathbf{r}') \frac{\mathbf{r}' - \mathbf{r}}{|\mathbf{r}' - \mathbf{r}|^3} dv', \tag{2}$$

where $\mathbf{r}$ is an observation point and integration is conducted over the variable $\mathbf{r}'$. The gravity field can be expressed by the gravity potential $U(\mathbf{r})$,

$$\mathbf{g}(\mathbf{r}) = \nabla U(\mathbf{r}), \tag{3}$$

where

$$U(\mathbf{r}) = \gamma \iiint_D \frac{\rho(\mathbf{r}')}{|\mathbf{r}' - \mathbf{r}|} dv'. \tag{4}$$

The second spatial derivatives of $U(\mathbf{r})$,

$$g_{\alpha\beta}(\mathbf{r}) = \frac{\partial^2}{\partial\alpha\partial\beta} U(\mathbf{r}), \quad \alpha, \beta = x, y, z, \tag{5}$$

form a gravity gradient tensor,

$$\hat{\mathbf{g}} = \begin{bmatrix} g_{xx} & g_{xy} & g_{xz} \\ g_{yx} & g_{yy} & g_{yz} \\ g_{zx} & g_{zy} & g_{zz} \end{bmatrix}, \tag{6}$$

where

$$g_{\alpha\beta} = \frac{\partial g_\alpha}{\partial\beta}, \quad \alpha, \beta = x, y, z. \tag{7}$$

The expressions for the gravity gradient tensor components can be calculated based on formulas (4) and (5):

$$g_{\alpha\beta}(\mathbf{r}) = \gamma \iiint_D \rho(\mathbf{r}') \frac{1}{|\mathbf{r}' - \mathbf{r}|^3} K_{\alpha\beta}(\mathbf{r}' - \mathbf{r}) dv', \tag{8}$$

where the kernels $K_{\alpha\beta}$ are equal to

$$K_{\alpha\beta}(\mathbf{r}' - \mathbf{r}) = \begin{cases} 3\dfrac{(\alpha - \alpha')(\beta - \beta')}{|\mathbf{r}' - \mathbf{r}|^2}, \alpha \neq \beta, \\ \qquad\qquad\qquad\qquad \alpha, \beta = x, y, z, \\ 3\dfrac{(\alpha - \alpha')^2}{|\mathbf{r}' - \mathbf{r}|^2} - 1, \alpha = \beta. \end{cases} \tag{9}$$

We also define the component

$$g_\Delta = \frac{1}{2}(g_{xx} - g_{yy}), \tag{10}$$

which can be measured using the Falcon AGG instrument, as discussed below.

Computing the gravity gradient tensor components

To derive numerical expressions for the 3D gravity field and gravity tensor, we divide the domain D, filled with the masses of a density $\rho(\mathbf{r}')$, into N_m cells D_k, $D = \cup_{k=1}^{N} D_k$, and assume that density is constant within each cell, $\rho(\mathbf{r}') = \rho_k$, $\mathbf{r}' \in D_k$:

$$g_z(\mathbf{r}) = \gamma \sum_{k=1}^{N_m} \rho_k \iiint_{D_k} \frac{z' - z}{|\mathbf{r}' - \mathbf{r}|^3}\, dv'. \tag{11}$$

The analytical formulas for computation of gravity field and gravity gradient fields from a rectangular prism are found in Forsberg (1984) and Li and Chouteau (1997). For example, Forsberg (1984) derives the equation for the vertical gravity gradient component of a cubic body:

$$g_{zz} = \gamma\rho \sum_{i=1}^{2}\sum_{j=1}^{2}\sum_{k=1}^{2} \mu_{ijk} \arctan \frac{x_i y_j}{z_k r_{ijk}}, \tag{12}$$

$$\mu_{ijk} = (-1)^i(-1)^j(-1)^k, \quad x_i = x - \xi_i,$$

$$y_j = y - \eta_j, \quad z_k = z - \varsigma_k,$$

where g_{zz} is the vertical gradient of g_z; ρ is the density of the cube; x, y, z are the observation points; and $\xi_i, \eta_j, \varsigma_k$ are the coordinates of the opposing vertices of the cube.

In our implementation of the inversion code, to speed up the computations, we use the simplified expressions for 3D gravity field and gravity tensor, based on the formulas derived for a point mass. We denote the coordinates of the cell center as $\mathbf{r}' = (x_k', y_k', z_k')$, $k = 1, \ldots, N_m$, and the cell sides as dx, dy, dz. Also, we have a discrete number of observation points $\mathbf{r}_n = (x_n, y_n, 0)$, $n = 1, \ldots, N_d$. Using discrete model parameters and discrete data, we can present the forward modeling operator for the gravity field [equation (11)] as

$$g_z(\mathbf{r}_n) \approx \sum_{k=1}^{N_m} A_{nk}^{g} \rho_k, n = 1, \ldots, N_d, \tag{13}$$

where the gravity field kernel A_{nk}^{g} according to equation (11) is expressed as

$$A_{nk}^{g} = \gamma \frac{z_k dx dy dz}{r_{nk}^3} \tag{14}$$

and

$$r_{nk} = \sqrt{(x_k' - x_n)^2 + (y_k' - y_n)^2 + (z_k')^2}. \tag{15}$$

We can apply the same technique to compute the gravity tensor components $g_{xz}, g_{yz}, g_{zz}, g_{xy}$, and g_Δ:

$$g_{\alpha\beta}(\mathbf{r}_n) \approx \sum_{k=1}^{N_m} A_{nk}^{\alpha\beta} \rho_k, n = 1, \ldots, N_m; \alpha, \beta = x, y, z, \tag{16}$$

where

$$A_{nk}^{\alpha\beta} = \gamma \frac{dx dy dz}{r_{nk}^3} K_{nk}^{\alpha\beta}, \tag{17}$$

$$K_{nk}^{\alpha\beta} = \begin{cases} 3\dfrac{(\alpha_k' - \alpha_n)(\beta_k' - \beta_n)}{r_{nk}^2}, \alpha \neq \beta, \\ \\ 3\dfrac{(\alpha_k' - \alpha_n)^2}{r_{nk}^2} - 1, \alpha = \beta, \end{cases} \quad \alpha, \beta = x, y, z. \tag{18}$$

The differential curvature component g_Δ is expressed as

$$g_\Delta(\mathbf{r}_n) \approx \sum_{k=1}^{N_m} A_{nk}^{\Delta} \rho_k, \tag{19}$$

where

$$A_{nk}^{\Delta} = 3\gamma \frac{(x_k' - x_n)^2 - (y_k' - y_n)^2}{2r_{nk}^5}\, dx\, dy\, dz. \tag{20}$$

Thus, the discrete forward modeling operators for the gravity field and gravity tensor can be expressed in general matrix notations as

$$\mathbf{d} = \mathbf{A}\mathbf{m}. \tag{21}$$

Here, $\mathbf{m}$ is a vector of the model parameters (densities, ρ_k) of the order N_m; $\mathbf{d}$ is a vector of the observed data $g_z, g_{xz}, g_{yz}, g_{zz}, g_{xy}$, and g_Δ of the order N_d; and $\mathbf{A}$ is a rectangular matrix of a size $N_d \times N_m$, formed by the corresponding gravity field kernels A_{nk}^{g}, $A_{nk}^{\alpha\beta}$, or A_{nk}^{Δ}.

Note that in the framework of this approach, we actually represent the subsurface model as a superposition of multiple point masses or of multiple small homogeneous balls with the volume equal to $dxdydz$. Application of these formulas for inversion means that we use these small balls as the building blocks for our inverse model instead of using rectangular prisms to describe the subsurface. The volume of the ball is equal to the volume of the corresponding rectangular cell. Thus, the choice of an appropriate formula for forward modeling, based on the analytical solutions for the rectangular prism or for the ball, determines the type of inverse model parameterization. Using the small ball parameterization speeds up all calculations dramatically.

At the same time, our numerical modeling and inversion results show that there is practically no difference in which parameterization to use if one considers a fine discretization of the area of inversion. Our method is based on dividing the subsurface region into many (up to hundreds of thousands) elementary cells (or equivalent elementary balls) and searching the physical properties of these cells using regularized inversion. This approach allows the most realistic interpretation of 3D potential field data in complex geological structures and at the same time generates an extremely fast and powerful computer code. Numeric examples, presented below, demonstrate that inversion of the practical gravity gradient data on a grid with about 100 000 cells can be done within 10 minutes on a PC with 1 GHz CPU. Note that the version of the code based on exact formula (12) for the elementary cubic cell produces practically the same result as the code based on simplified expressions (17), but the computations require more time.

Gravity curvature

The components g_{zx} and g_{zy} represent the horizontal gradients of the gravity field g_z, while the component g_{zz} is its

vertical gradient. The components g_{xy} and g_{Δ} are called the differential curvature components because they determine the curvature of the equipotential surface of the gravity potential. The geometric properties of these components were investigated many decades ago in papers on torsion balance measurements (e.g., Rybár, 1923; Slotnick, 1932; Heiland, 1946; Jakosky, 1950). However, we feel it is important to review some of these properties and the physical interpretation of the differential curvature components, as they can now be measured by the Falcon AGG. In our explanation we mainly follow the work of Slotnick (1932).

To understand better the relationship between the gradients of the gravity field and the geometrical properties of the equipotential surface, we use a special coordinate system in this section. The origin of this system is located in the observation point, the z-axis is directed along the normal vector to the equipotential surface, and the x- and y-axes are located in the tangential plane to the equipotential surface.

In this coordinate system, the curvature C of the normal section of the equipotential surface is determined by the equation

$$C = C(\varphi) = -\frac{1}{g_z}\left(g_{xx}\cos^2\varphi + g_{xy}\sin 2\varphi + g_{yy}\sin^2\varphi\right), \tag{22}$$

where φ is an angle between the vertical plane xz and the given normal section. The principal normal sections are characterized by maximal or minimal curvature. We can find the angles of the principal normal sections from the condition

$$\frac{\partial C(\varphi)}{\partial \varphi} = 0. \tag{23}$$

Differentiating equation (22), we obtain the following equation for the angle φ_0 of the principal normal section:

$$g_{\Delta}\tan 2\varphi_0 = g_{xy}. \tag{24}$$

Note that equation (24) has two solutions, φ_0 and $\varphi_1 = \varphi_0 + \pi/2$, which correspond to two principal normal sections of the equipotential surface. We denote by $R_{\min}$ and $R_{\max}$ the radii of the adjusting circles to the corresponding normal sections (Figure 2).

Let φ_0 be an angle corresponding to the normal section with the maximum curvature $C(\varphi_0) = C_{\max} = 1/R_{\min}$. The second principal normal section has the minimum curvature $C(\varphi_1) = C(\varphi_0 + \pi/2) = C_{\min}$. Let us calculate the difference ΔC of the maximum and minimum curvatures:

$$\begin{aligned}\Delta C &= C_{\max} - C_{\min} \\ &= -\frac{1}{g_z}(2g_{\Delta}\cos 2\varphi_0 + 2g_{xy}\sin 2\varphi_0).\end{aligned} \tag{25}$$

Now we introduce the notation

$$G = \Delta C\, g_z,$$

where G is the so-called gravity curvature. Substituting equation (24) into equation (25) and with some rearrangements, we can obtain the result that the differential curvature components g_{Δ} and g_{xy} are proportional to the gravity curvature G:

$$g_{\Delta} = -\left(\frac{G}{2}\right)\cos 2\varphi_0, \quad g_{xy} = -\left(\frac{G}{2}\right)\sin 2\varphi_0 \tag{26}$$

and

$$g_{\Delta}^2 + g_{xy}^2 = \frac{G^2}{4}. \tag{27}$$

For a spherical surface, ΔC is equal to zero for any point on the surface. Therefore, G can be treated as the measure of the deviation of the equipotential surface at a given point from a spherical surface, which is typical for a gravity potential of a point mass. Thus, the gravity gradient tensor components g_{Δ} and g_{xy}, which are proportional to G, reflect the deviation of the density distribution from the elementary point source, located under the point of observation. Note that these components are measured by the Falcon AGG.

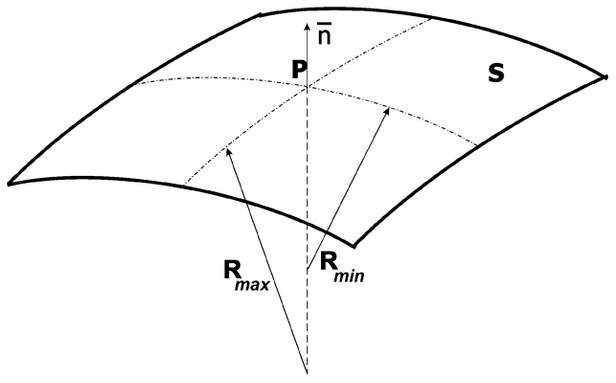

Figure 2. Two principal normal sections of the equipotential surface. The gravity curvature is proportional to the difference, $\Delta C = C_{\max} - C_{\min} = (1/R_{\min}) - (1/R_{\max})$.

PRINCIPLES OF REGULARIZED INVERSION OF GRAVITY AND GRAVITY GRADIENT TENSOR DATA

Gravity gradient tensor component data inversion is reduced to the solution of the linear matrix equation (21). This inverse problem is ill posed, i.e., the solution can be nonunique and unstable. Therefore, we have to use the methods of regularization theory to solve this problem (Tikhonov and Arsenin, 1977; Zhdanov, 2002). In the conventional way, we substitute the solution of the linear inverse problem [equation (21)] with the minimization of the Tikhonov parametric functional

$$P^{\alpha}(\mathbf{m}) = \phi(\mathbf{m}) + \alpha s(\mathbf{m}) = \min, \tag{28}$$

where the misfit functional is specified as

$$\phi(\mathbf{m}) = \|\mathbf{W}_d(\mathbf{A}\mathbf{m} - \mathbf{d})\|^2. \tag{29}$$

Here, α is a regularization parameter, $\mathbf{W}_d$ is the data weighting matrix, and $\mathbf{m}$ is a vector of anomalous density distribution.

There are different ways of introducing a stabilizing functional. The traditional inversion algorithms are usually based on the minimum norm, or smoothing stabilizing functionals (e.g., Li and Oldenburg, 1996). These algorithms have difficulties, however, in describing the sharp geological boundaries between different geological formations. This problem arises, for example, in inversion for the local target with sharp boundaries between the ore zone and the host rocks, which is a typical model in mining exploration. In these situations, it is useful to search for a stable solution within the class of inverse models with sharp geological boundaries. The solution of this problem

is based on introducing a special type of stabilizing functional, the so-called minimum support or minimum gradient support functionals (Portniaguine and Zhdanov, 1999, 2002; Zhdanov, 2002). We select a stabilizer equal to the minimum support functional:

$$s(\mathbf{m}) = s(m_1, m_2, \ldots, m_{N_m}) = \sum_{k=1}^{N_m} \frac{m_k^2}{m_k^2 + e}, \quad e > 0, \tag{30}$$

where e is a focusing parameter determining the sharpness of the produced image (Zhdanov, 2002).

The minimization problem (28) is solved using the reweighted regularized conjugate gradient (RRCG) method, outlined in previous publications (Portniaguine and Zhdanov, 1999, 2002). The reader can find a detail explanation of this algorithm in Zhdanov (2002, 155–165).

Using the gradient data jointly with the gravity data reduces the ambiguity and increases the resolution of inversion (Jorgensen and Kisabeth, 2000; Routh et al., 2001). It is not so difficult to construct the method of joint gravity and gravity tensor data inversion by combining in the data vector $\mathbf{d}$ the different components of the gravity field and its tensor. For example, one can run the joint inversion of the differential curvature components g_{xy} and g_Δ by constructing $\mathbf{d}^{xy,\Delta}$ of the order $2N_d$ as a combination of the g_{xy} and g_Δ values at the observation points,

$$\mathbf{d}^{xy,\Delta} = \left[g_{xy}(\mathbf{r}_1), \ldots, g_{xy}(\mathbf{r}_{N_d}), g_\Delta(\mathbf{r}_1), \ldots, g_\Delta(\mathbf{r}_{N_d})\right], \tag{31}$$

and introducing rectangular $2N_d \times N_m$ matrix $\mathbf{A}$ formed by the corresponding gravity field kernels A_{nk}^{xy} and A_{nk}^{Δ}:

$$\mathbf{A}^{xy,\Delta} = \begin{bmatrix} \mathbf{A}^{xy} \\ \mathbf{A}^{\Delta} \end{bmatrix}, \tag{32}$$

where $N_d \times N_m$ matrices $\mathbf{A}^{xy}$ and $\mathbf{A}^{\Delta}$ are

$$\mathbf{A}^{xy} = \left[A_{nk}^{xy}\right], \quad \mathbf{A}^{\Delta} = \left[A_{nk}^{\Delta}\right],$$
$$n = 1, \ldots, N_d; \quad k = 1, \ldots, N_m. \tag{33}$$

The joint inversion is reduced now to the solution of the matrix equation

$$\mathbf{d}^{xy,\Delta} = \mathbf{A}^{xy,\Delta}\mathbf{m}. \tag{34}$$

In a similar way, we can introduce a matrix equation for the joint inversion of any combination of the gravity and gravity gradiometer data. The stable solution of these equations is based on the same RRCG method (Zhdanov, 2002).

NUMERICAL MODELING RESULTS AND DISCUSSION

The forward modeling and the inversion code have been developed using Matlab. To check for the validity of the code and the inversion method, we used for inversion the data generated for a simple model. Figure 3 shows two cubic bodies, each $150 \times 150 \times 150$ m and with a density contrast of 10^3 kg/m^3 over the background. The top of the bodies is located 150 m below the surface. The gravity field g_z and gravity tensor components g_{zz}, g_{xy}, and g_Δ were generated by the forward modeling code with $525 = 21 \times 25$ observation points of the rectangular grid located at the earth's surface. The sampling interval is 25 m in the x- and y-directions. The synthetic observed data were contaminated with 3% noise and were used for inversion. As an example, the left panels in Figure 4 show the differential curvature tensor components g_{xy} and g_Δ, respectively. One can see that, even for this simple model, the maps of the tensor components of the gravity field have rather complicated structures, which makes it difficult to provide a qualitative interpretation of these maps.

The area of inversion was discretized into $11 \times 13 \times 10 = 1430$ cubic cells in the x-, y-, and z-directions, respectively. The size of a cubic cell is 50 m along the x-, y-, and z-directions. Our inversion code, as pointed out earlier, has options of smooth and focusing inversion. The models generated by the smooth inversion of the gravity field g_z and gravity tensor components g_{zz}, g_{xy}, and g_Δ are shown in Figure 5; the models obtained by the focusing inversion are shown in Figure 6. All inversions were run until the misfit between the predicted and observed data reached 3% (the noise level in the data). In the case of focusing inversion, a priori information about the density distribution, which is used as bounding values in inversion, is important. In obtaining the results shown in this section, we applied a lower bound for anomalous density of -0.1×10^3 kg/m^3 and an upper bound of 10^3 kg/m^3.

As an example, the corresponding predicted data for the models generated by the focusing inversion are shown in the right panels of Figure 4. For all components, the focusing inversion result can resolve the sharp boundary structures of the anomalous bodies over the background, while the smooth inversion cannot resolve two bodies. This is in spite of the fact that the predicted data for the smooth models fit the observed data with the same accuracy as for the focused models. Also, it is evident from the figures that the gravity field g_z provides a poorer recovery of the original model, whereas g_Δ, g_{xy}, and g_{zz} and the joint inversion of g_{xy} and g_Δ represent the bodies practically at the original position and with the correct density contrast.

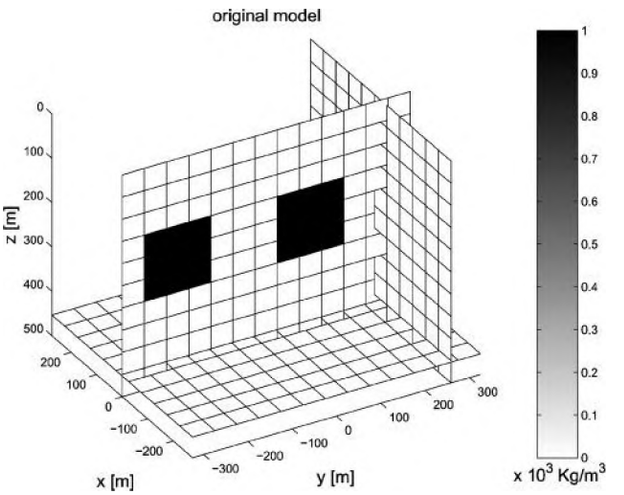

Figure 3. Vertical slice of a model with two cubic bodies, each $150 \times 150 \times 150$ m, and a density contrast of 10^3 kg/m^3 over the background, The distance between two bodies is 150 m.

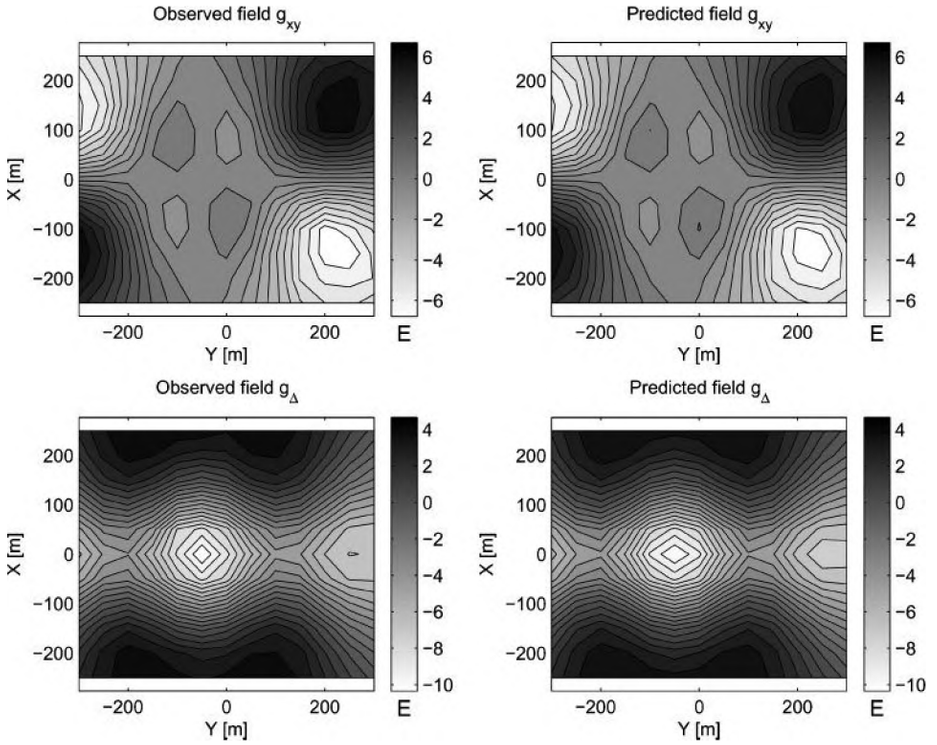

Figure 4. (left) Maps of the g_{xy} and g_{Δ} component contaminated by 3% Gaussian noise, used as observed data for inversion. (right) Predicted data, computed for the model obtained with the focusing inversion.

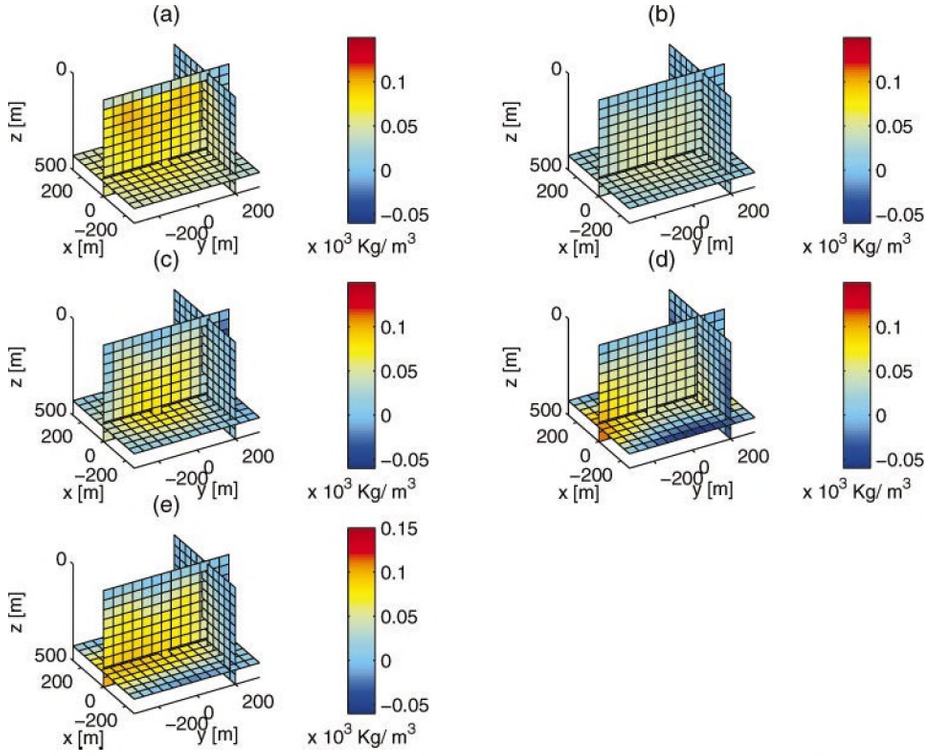

Figure 5. The models generated by (a) the smooth inversion of gravity field g_z, (b) gravity tensor components g_{zz} (c) g_{xy}, (d) g_{Δ}, and (e), joint inversion of the differential curvature components g_{xy} and g_{Δ} with the misfit between the predicted and observed data equal to 3% (the noise level in the data). The bodies are not resolved clearly in these images.

INTERPRETATION OF GRADIENT GRAVITY DATA IN THE CANNINGTON AG-PB-ZN OREBODY IN QUEENSLAND, AUSTRALIA

Geological background

The Cannington deposit is located within the eastern succession of the Proterozoic Mount Isa inlier, northwest Queensland, as shown in Figure 7. The deposit is concealed beneath 10 to 60 m of Cretaceous and Recent sediments and was discovered by BHP Minerals in 1990 as a result of drill testing regional magnetic targets. The Cannington deposit is hosted by a sequence of magmatic, biotite-sillimanite-garnet-bearing quartzofeldspathic gneisses with minor amphibolites. A distinctive sequence of biotite-sillimanite schists and feldspathic psammites with layers and disseminations of fine-grained manganese (Mn) almandine garnets extends for up to 250 m as an envelope around the main mineralized zone. Economic Ag-Pb-Zn mineralization at Cannington is associated with a remarkably diverse range of siliceous and iron/calcium/manganese/fluorine lithologies characterized by coarse-grained equigranular textures (Walters and Bailey, 1998). The strong zonations between silver/lead- and zinc-rich mineralization types are a feature of the deposit. The high silver grades that are characteristic of the deposit are largely related to argentiferous galena with abundant inclusions of freibergite.

The overall geometry of the deposit appears to be controlled by a tight to isoclinal synform that strikes north–south, dips from 40°–70° to the east, and plunges to the south. A large amphibolite body, called the Core Amphibolite, occurs within the axial trace of this interpreted synform and is used to define footwall versus hanging-wall orebody zones (Figure 7). The deposit is divided by faulting into a shallow, low-grade northern zone and a deeper, higher grade, and more extensive southern zone. The density of the host gneiss is 2.6–2.7 $\times 10^3$ kg/m^3, and local amphibolites attain a density of 3.0 $\times 10^3$ kg/m^3. The mineralized orebody zones have a density of 3.5 $\times 10^3$ kg/m^3, which means the anomalous density over the background should not be higher than 10^3 kg/m^3.

The AGG instrument

BHP Billiton's Falcon™ AGG is a result of a feasibility study and development program carried out by BHP and Lockheed Martin between 1991 and 2000. The AGG accelerometers are of the force rebalance type. In these accelerometers the position of a proof mass pendulum is sensed by a capacitance bridge circuit, and a force is applied to maintain the pendulum at a position to null the bridge (Metzger, 1982).

The exact design of the Falcon AGG is proprietary; however, schematically in an AGG the four accelerometers are mounted

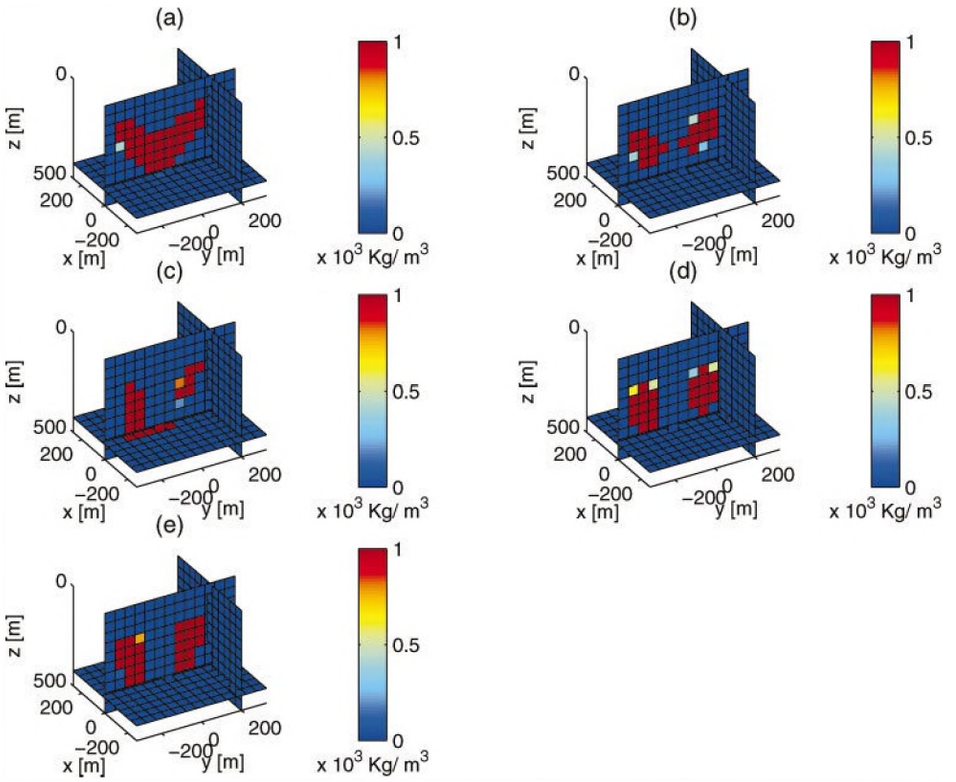

Figure 6. The models generated by (a) the focusing inversion of gravity field g_z, (b) gravity tensor components g_{zz}, (c) g_{xy}, (d) g_Δ, and (e) joint inversion of the differential curvature components g_{xy} and g_Δ with the misfit between the predicted and observed data equal to 3% (the noise level in the data). We can see the reasonable images of the model in this case.

to a rotor so they are equispaced on a circle, with their sensitive axes tangential to the circle with the same sense. The rotor rotates at a constant speed, typically $\Omega = 0.25$ rad/s, providing a further ability for common mode rejection. The four AGG accelerometers form a complement, and their outputs are combined (summed) so that orthogonal accelerometers have opposite sense and opposed accelerometers have the same sense as shown in Figure 2. Linear accelerations perpendicular to the spin axis are modulated at the rotation frequency. Gravity gradient accelerations are modulated at twice the rotation frequency because the radius arm and the in/out axes are each modulated at rotation frequency with respect to the fixed coordinate system (Metzger, 1982). Ideally (noise free), the output of this accelerometer complement is

$$4R[\sin(2\Omega t)g_{xy} + \cos(2\Omega t)g_{\Delta}], \tag{35}$$

where R is the radius of the complement, Ω is the rotation rate (rad/s), t is the time, and g_{xy} and g_{Δ} are the corresponding differential curvature components of the gravity tensor. These components are therefore separated in the frequency domain from the instrument bias and linear accelerations, which allows the demodulation technique to detect extremely small gravity gradient signals, required for exploration (Lee, 2001).

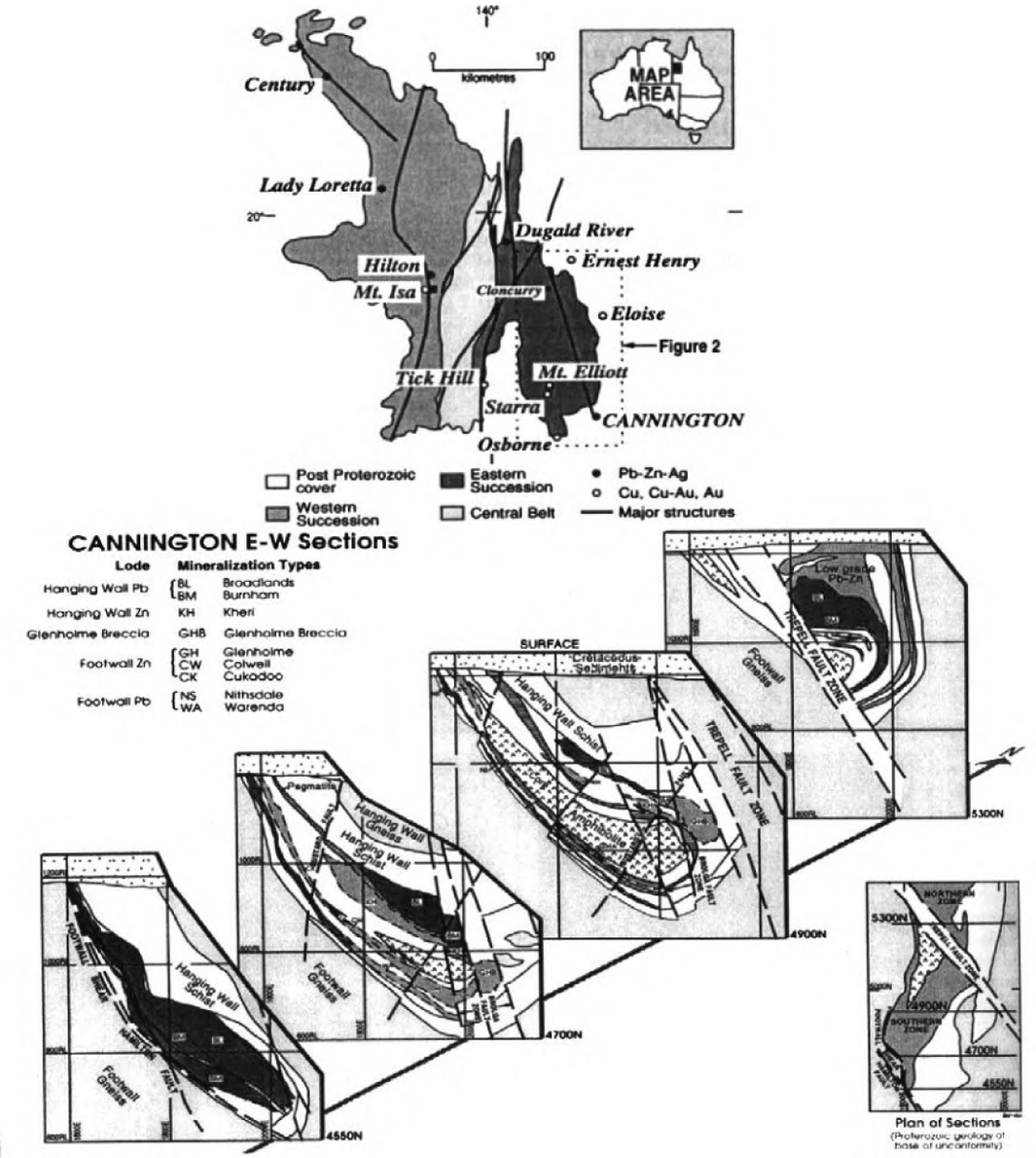

Figure 7. A geological map showing (top) the location of the Cannington deposit in the northwestern corner of Queensland and (bottom) the geological structure of the Cannington deposit, interpreted from drilling and magnetic survey data (after Walters and Bailey, 1998).

Bell Aerospace originally developed the tensor system, not the two-component system. The tensor system is now commercially used by Bell Geospace in both marine and airborne surveys (see www.bellgeo.com for details). Therefore, all components of the gravity gradient tensor can be measured by the airborne survey. At the same time, our interpretation technique can be applied to all tensor components as well. However, in this section we consider interpretation of the Falcon™ AGG data only.

AGG survey and data interpretation

In April 2000, BHP Billiton conducted an AGG test survey over the Cannington Ag-Pb-Zn orebody. To test the inversion, a 4×4-km section of processed data was extracted from the complete survey data set. The observed data along 41 survey lines within this area were inverted. The processed data, in this case, corresponded to an effective sensor height of 120 m above mean ground level with sampling approximately every 20 m along survey lines. The separation between the survey lines was 100 m. All together, the number of data points was 7814. The survey aircraft included a stinger magnetometer, global positioning system (GPS) positioning, a laser scanner, and optionally radiometric crystals, eliminating the need for extra surveys for necessary or complementary data. Acquisition of the laser scanner data was essential to generate a digital terrain model used to remove the topographic contribution to the gravity gradient data. The observed AGG data were corrected for residual aircraft acceleration effects as well as demodulation and filtering of the modulated tensor components. Following the demodulation process, a number of deterministic corrections were applied to the observed data; these included corrections for the gravitational effects of the aircraft frame and platform masses as well as terrain corrections. In addition, the differential curvature tensor components were transformed to the vertical gravity gradient g_{zz} and the vertical gravity component g_z.

The area of inversion was discretized into $80 \times 86 \times 15 = 103\,200$ rectangular cells in the x-, y-, and z-directions, respectively. The size of a rectangular cell was 50 m along the x- and y-directions (north–south and east–west, respectively) and 40 m in the z-direction. Therefore, the total depth of inversion was 600 m from the surface.

The gravity tensor inversion code included options for inverting g_{zz}, g_{xy}, and g_Δ in addition to g_z, as well as joint inversion of the different gravity gradient tensor components. To check for the noise in the data, g_{xy} and g_Δ were inverted and the resulting models were then used to predict fields g_z and g_{zz}. These were then compared with the original fields obtained by the numerical transformation of fields g_{xy} and g_Δ observed from the AGG survey. Furthermore, the same procedure was carried out for a joint inversion of g_{xy} and g_Δ. The data were made to reach a misfit of under 3%. For reasons discussed in the section on geologic background, the material property constraints were set between -0.1×10^3 kg/m^3 and 10^3 kg/m^3. The results are shown in Figures 8 and 9. The comparisons immediately show that the predicted fields fit the observed data extremely accurately. Note that it took only about 10 minutes on a PC with a 1-GHz CPU to invert one component of the gravity gradient tensor.

Figure 8a presents the original field g_z obtained by numerically transforming the observed tensor components g_{xy} and g_Δ. There exists an approximately linear regional southeast–northwest trend of increasing density that corresponds to the existence of the Trepell fault, which is about 100 m wide, characterized by a low-density clay chlorite gouge. Just north of the fault is a sudden high-density anomaly that corresponds to the orebody. To accentuate the presence of this orebody further, this linear trend is removed from the data using a linear least-squares fit for the data and subtracting the best-fit plane from the observed field. The resultant observed field is shown in Figure 8b. One can see a strong anomaly around the central part of the surveyed area. We then invert this processed data using regularized focusing inversion code. Figure 10 presents the vertical slices of the model constructed by our inversion method, showing the depth and the extent of the orebody. The

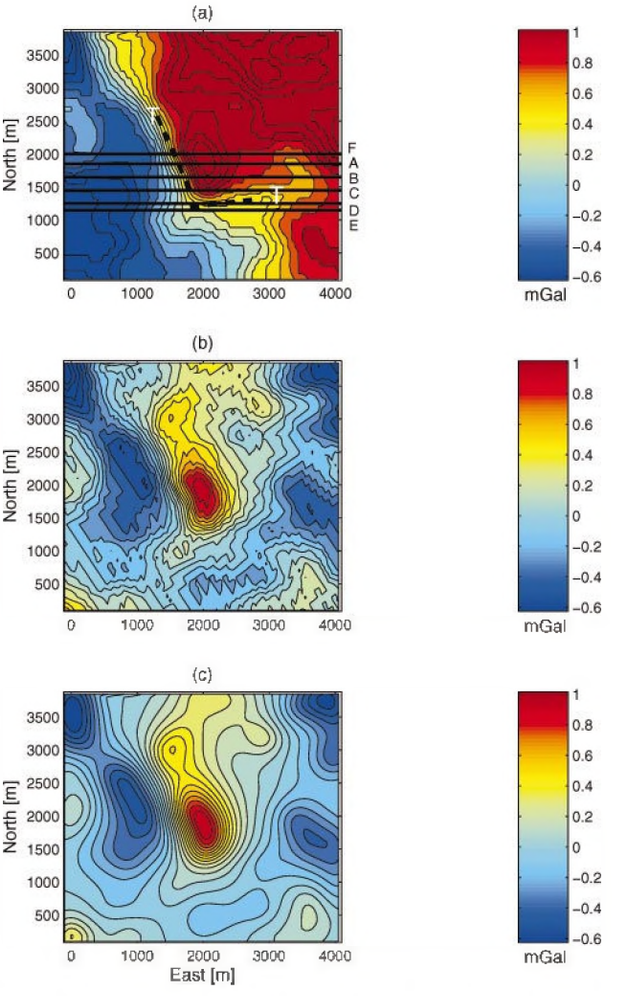

Figure 8. (a) The original field g_z obtained by numerically transforming the observed tensor components g_{xy} and g_Δ. (b) The same data with the removed linear trend. (c) The predicted data g_z for the model obtained by inversion of the data shown in (b). The letters A, B, C, D, and F denote the profiles used to construct the vertical slices of the inversion results. The crooked heavy dashed line in (a) shows the position of the Trepell fault.

anomalous body tapers and thins out progressively southward. The sections through *CC* and *DD* apparently show the existence of another anomalous body about 2 km away from the former, which is found to be buried at greater depth. Walters and Bailey (1998) mention the existence of multiple bodies on the southern side of the fault. This seems to be confirmed by our inversion results. Also, the orebody has an envelope of low-density material around it. This seems to be the distinctive sequence of biotite-sillimanite schists and feldspathic psammites with layers and disseminations of fine-grained manganese almandine garnets extending for up to 250 m as an envelope around the main mineralization zone.

The tensor component g_{zz} suggests a similar finding but seems to constrain and focus the anomaly over a narrower region, as shown in Figure 9a. The regional linear trend is not present, and the central anomaly is readily visible. The Trepell fault is delineated significantly better here than in the g_z map. The vertical slices of Figure 11 represent the results of the g_{zz} component inversion, and the extent of the anomalous body is more sharply defined. The presence of the orebody on the southern side of the fault shows up at a greater depth, as is expected from the local geology (Christensen et al., 2001). The other geological features mentioned while describing the images for g_z are all shown here. The theoretical predicted data g_{zz} for this model are shown in Figure 9b. The observed differential curvature components g_{xy} and g_Δ are shown in Figures 9c and 9e, respectively. The Trepell fault is very clearly delineated in the map of g_{xy}.

Figure 12 presents the slices obtained as a result of the joint inversion of g_{xy} and g_Δ. The sections as indicated in Figure 12 show the orebody at more or less the same location as for g_{zz}. However, in the more southern sections, as the fault zone is reached, the density contrast against the background is more pronounced compared to the results obtained from the g_{zz} data. Figure 13 shows the horizontal slices of the model obtained by the joint focusing inversion of g_{xy} and g_Δ components at a depth of 100, 200, and 300 m, respectively. Based on our experience of numerical modeling and also because of the sensitivity of the gravity curvature components to lateral density variations as discussed earlier, the positions of the anomalies as shown in these figures are considered to be the closest to the true subsurface density variations. The theoretical predicted data for this model are shown in Figures 9d and 9f, respectively. The predicted data fit the observed data with the misfit less than 3%.

Comparison with drilling results

We have compared the model obtained by the regularized focusing inversion of the differential curvature components

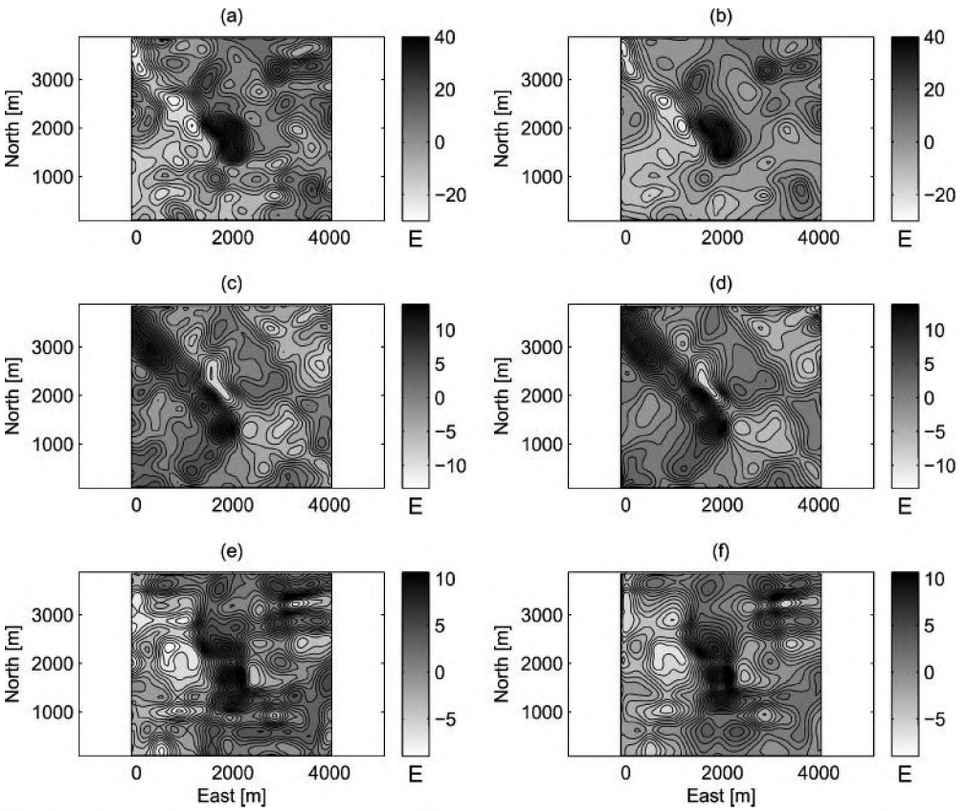

Figure 9. (a) Map of the original tensor component g_{zz}, obtained by numerically transforming the observed tensor components g_{xy} and g_Δ. (b) Predicted data g_{zz} for the model obtained by inversion of the data shown (a). The maps of the observed tensor component g_{xy} and g_Δ are shown in panels (c) and (e), respectively. (d), (f) The predicted data g_{xy} and g_Δ for the models obtained by inversion of the data shown in (c) and (e), respectively.

with the drilling data. As an example, we present profiles EE and FF of Figure 8 (top panel), which are indicative of true subsurface conditions as inferred from drilling data, provided by BHP Billiton after the numerical inversion was completed. Figure 14 shows the vertical sections along these profiles of the model obtained by the joint focusing inversion of g_{xy} and g_{Δ} components. We also compare in this figure the gravity gradient tensor inversion result with the geological model constructed by BHP Billiton based on the known geology and the drilling results. While in Figure 14a the orebody is linear and dipping (lead load is shown by the dashed red zones), the focusing inversion result on the background is capable of picking a blocky density anomaly up to 150 m depth only. Note, however, that profile EE crosses the orebody at the very southern edge, which makes it difficult for inversion to pick up a true deep structure of the body along this section. On the other hand, profile FF passes just above the center of the body. As a result, the blocky orebody and the anomalous density coincide almost completely in the vertical section passing through this profile (Figure 14b). This is to be expected since focusing inversion works on minimizing the area in which the anomaly is present, and whenever there is a concentration of anomalous mass, such inversion technique will definitely be able to localize it. One can see excellent matching between the inversion and the true

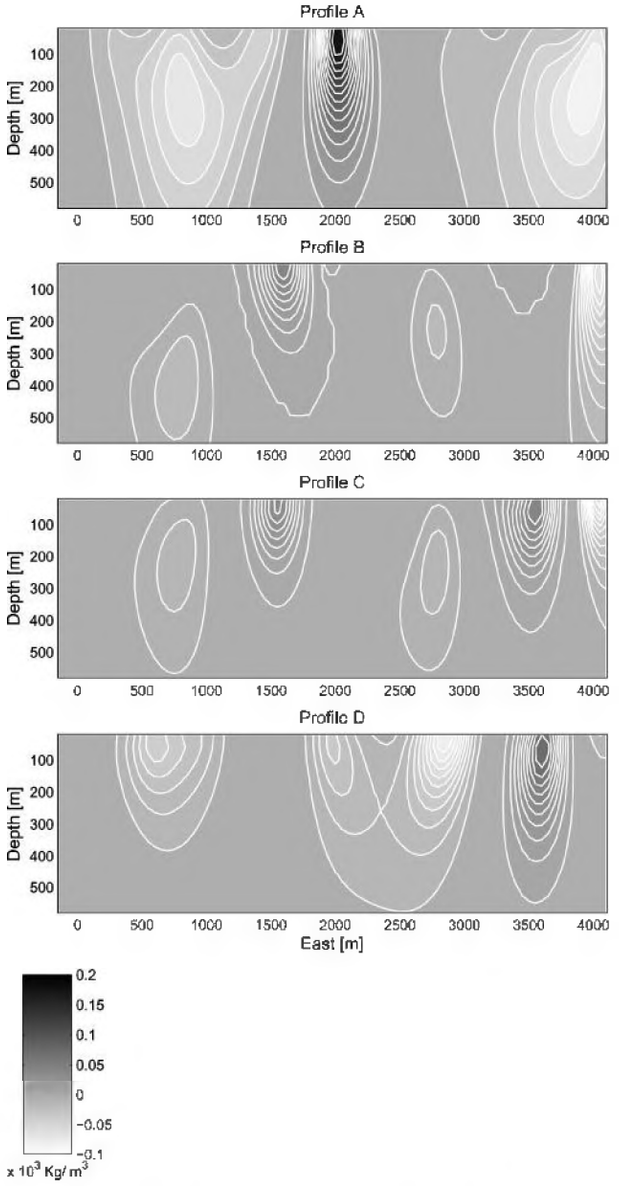

Figure 10. The vertical slices along profiles A, B, C, and D of the model obtained by inversion of component g_z. The inversion image picks up the density anomalies on either side of the fault but places them at shallower depth.

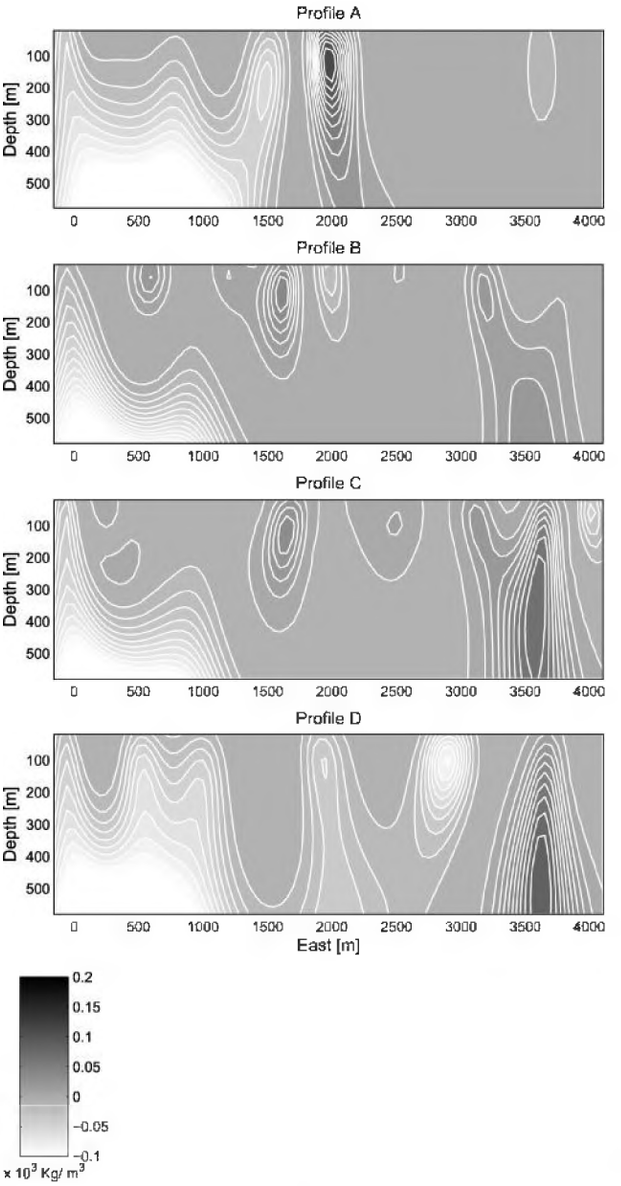

Figure 11. The vertical slices along profiles A, B, C, and D of the model obtained by inversion of component g_{zz}. The location of the top of the anomalies is nearer to correct depth. The base, however, is not well resolved.

geological data in Figure 14b, where the known mineralization is shown by the dashed red zone.

CONCLUSIONS

We have developed a method of gravity gradient tensor interpretation based on the focusing inversion technique introduced by Portniaguine and Zhdanov (1999) for vertical gravity component data inversion. The numerical modeling and inversion results show that the resolution of the gravity method can be improved significantly if we use the tensor gravity data for interpretation. The differential curvature tensor components g_{Δ} and g_{xy} have better lateral and vertical resolution than the vertical component of the gravity field g_z, which is measured in conventional gravity surveys. This conclusion seems to be obvious based on the fact that gradients represent shorter spatial wavelengths caused by shallower and narrower sources. Nevertheless, it is important to see the practical confirmation of this theoretical fact in the results of inversion of the gravity gradiometer data. We should note also that the better resolution can be obtained only when we are able to measure the gradient data with the appropriate accuracy, as discussed by Li (2001c).

We have also applied our new method for inversion of the gradient gravity data collected by BHP Billiton over the Cannington Ag-Pb-Zn orebody in Queensland, Australia. The comparison with the drilling results demonstrates a remarkable correlation between the density anomaly reconstructed by the gravity gradient data and the true structure of the orebody. This result indicates that the emerging new geophysical technology of the airborne gravity gradient tensor observations can

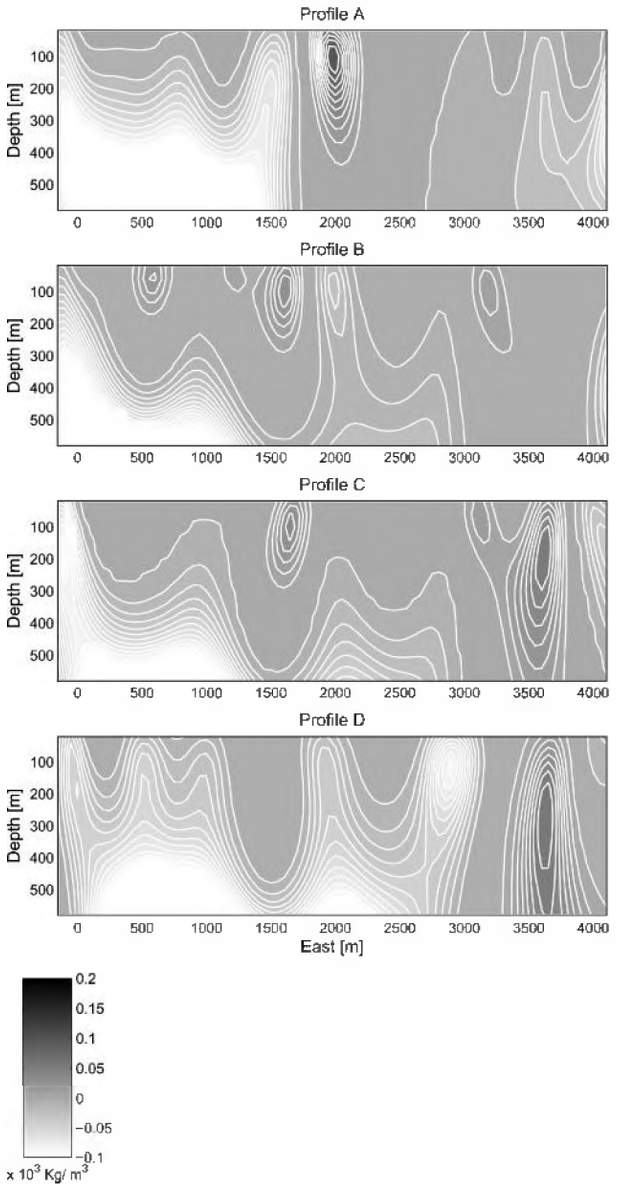

Figure 12. The vertical slices along profiles A, B, C, and D of the model obtained by the joint inversion of the differential curvature components g_{xy} and g_{Δ}. The position of the density anomalies is considered to be the closest to the true subsurface density variations.

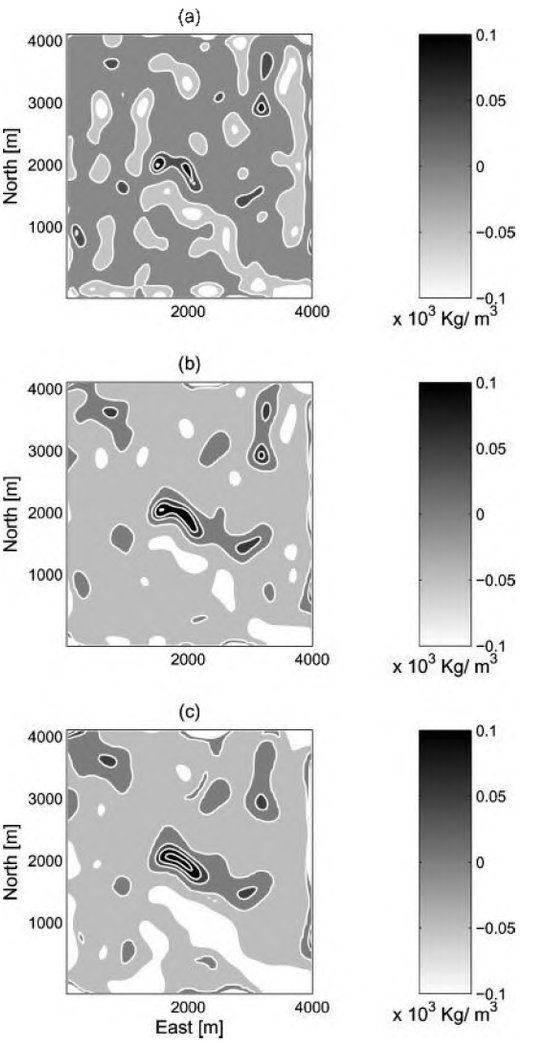

Figure 13. The Horizontal slices of the model obtained by the joint focusing inversion of components g_{xy} and g_{Δ} at a depth of (a) 100 m, (b) 200 m, and (c) 300 m.

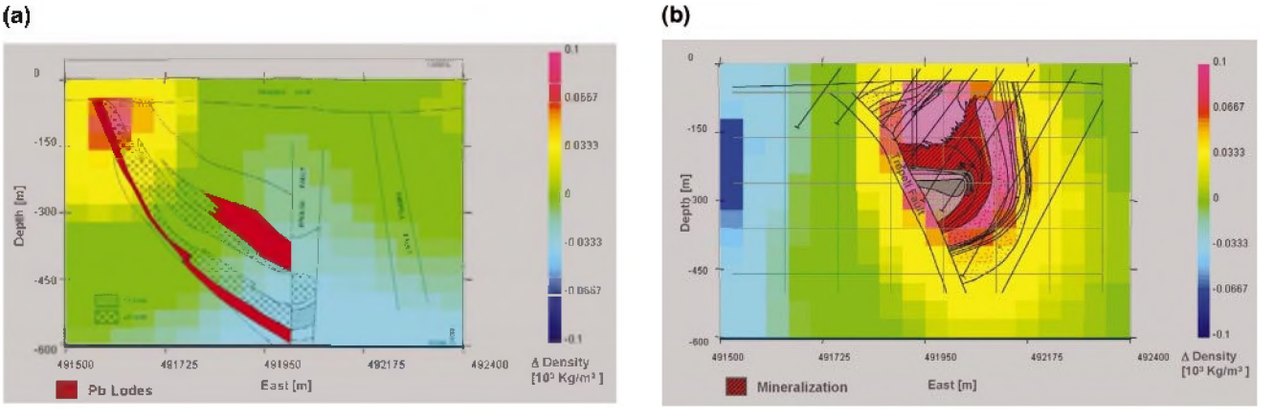

Figure 14. Comparison of the gravity gradient tensor inversion result with the geological model constructed by BHP Billiton based on the known geology and the drilling results for vertical sections along (a) profile *EE* and (b) profile *FF*.

significantly improve the practical effectiveness of the gravity method in mineral exploration.

ACKNOWLEDGMENTS

The authors acknowledge the support of the University of Utah Consortium for Electromagnetic Modeling and Inversion (CEMI), which includes Baker Atlas Logging Services, BHP Billiton, Electromagnetic Instruments Inc., ExxonMobil Upstream Research Company, INCO Exploration, International Energy Services, Japan National Oil Corporation, MINDECO, Naval Research Laboratory, Rio Tinto-Kennecott, Schlumberger Oilfield Services, Shell International Exploration and Production Inc., and Sumitomo Metal Mining Company. We are thankful to BHP Billiton for providing the real gravity gradiometer data and permission to publish the results. We would also like to thank Xiong Li for many useful comments and suggestions, which helped to improve the final version of the manuscript.

REFERENCES

Bell, R. E., and Hansen, R. O., 1998, The rise and fall of early oil field technology: The torsion balance gradiometer: The Leading Edge, **17**, 81–83.

Christensen, N. A., Mahanta, A., Boggs, D. B., and Dransfield, M. H., 2001, Falcon airborne gravity gradiometer survey results over the Cannington Ag-Pb-Zn deposit: Presented at the 15th Geophysical Conference and Exhibition, Australian Society of Exploration Geophysicists.

Condi, F., and Talwani, M., 1999, Resolution and efficient inversion of gravity gradiometry: 69th Annual International Meeting, Society of Exploration Geophysicists, Expanded Abstracts, 358–361.

Forsberg, R., 1984, A study of terrain corrections, density anomalies, and geophysical inversion methods in gravity field modeling: Report 355, Department of Geodetic Science and Surveying, The Ohio State University.

Heiland, C. A., 1940, Geophysical exploration: Prentice-Hall, Inc.

Jakosky, J. J., 1950, Exploration geophysics, 2nd ed.: Trija Publishing Company.

Jorgensen, G. J., and Kisabeth, J. L., 2000, Joint 3-D inversion of gravity, magnetic and tensor gravity fields for imaging salt formations in the deep water Gulf of Mexico: 70th Annual International Meeting, Society of Exploration Geophysicists, Expanded Abstracts, 424–426.

Lee, J. B., 2001, FALCON gravity gradiometer technology: Exploration Geophysics, **32**, 247–250.

Li, Y., 2001a, Processing gravity gradiometer data using an equivalent source technique: 71st Annual International Meeting, Society of Exploration Geophysicists, Expanded Abstracts, 1466–1469.

———2001b, 3-D inversion of gravity gradiometer data: 71st Annual International Meeting, Society of Exploration Geophysicists, Expanded Abstracts, 1470–1473.

Li, X., and Chouteau, M., 1997, Three-dimensional gravity modeling in all space: Surveys in Geophysics, **19**, 339–368.

———2001c, Vertical resolution: Gravity versus vertical gravity gradient: The Leading Edge, **8**, 901–904.

Li, Y., and Oldenburg, D., 1996, 3-D inversion of magnetic data: Geophysics, **61**, 394–408.

Metzger, E. H., 1977, Recent gravity gradiometer developments: Presented at Guidance and Control Specialist Conference, American Institute of Astronauts and Aeronautics.

———1982, Development experience of gravity gradiometer system: IEEE Plans, 323–332.

Pawlowski, B., 1998, Gravity gradiometry in resource exploration: The Leading Edge, **17**, 51–52.

Portniaguine, O., and Zhdanov, M. S., 1999, Focusing geophysical inversion images: Geophysics, **64**, 874–887.

———2002, 3-D magnetic inversion with data compression and image focusing: Geophysics, **67**, 1532–1541.

Routh, P., Jorgensen, G. J., and Kisabeth, J. L., 2001, Base of the salt imaging using gravity and tensor gravity data: 70th Annual International Meeting, Society of Exploration Geophysicists, Expanded Abstracts, 1482–1484.

Rybár, S., 1923, The Eötvös torsion balance and its application to the finding of mineral deposits: Economic Geology, **18**, 639–662.

Shaw, H., and Lancaster-Jones, E., 1923, Eötvös torsion balance: Proceedings of the Physical Society of London.

———1927, The theory and practical use of the Eötvös torsion balance: Mining Magazine, **35**, 151–166.

Slotnick, M. M., 1932, Curvature of equipotential surfaces: AAPG Bulletin, **16**, 1250–1259.

Tikhonov, A. N., and Arsenin, V. Y., 1977, Solution of ill-posed problems: V. H. Winston and Sons.

van Leeuwen, E. H., 2000, BHP develops airborne gravity gradiometer for mineral exploration: The Leading Edge, **19**, 1296–1297.

Walters, S., and Bailey, A., 1998, Geology and mineralization of the Cannington Ag-Pb-Zn deposit: An example of Broken Hill-type mineralization in the Eastern Succession, Mount Isa inlier, Australia: Economic Geology, **93**, 1307–1329.

Zhdanov, M. S., 1988, Integral transforms in geophysics: Springer-Verlag.

———2002, Geophysical inverse theory and regularization problems: Elsevier Science Publishing Co., Inc.

Zhdanov, M. S., Ellis, R. G., Mukherjee, S., and Pavlov, D. A., 2002, Regularized focusing inversion of 3-D gravity tensor data: 72nd Annual International Meeting, Society of Exploration Geophysicists, Expanded Abstracts, 751–754.